

Metrological Assessment of Quantum Anomalous Hall Properties

Linsey K. Rodenbach,^{1,2,3} Alireza R. Panna,¹ Shamith U. Payagala,¹ Ilan T. Rosen,^{3,4}
Molly P. Andersen,^{3,5} Peng Zhang,⁶ Lixuan Tai,⁶ Kang L. Wang,⁶ Dean G. Jarrett^{⊗,1},
Randolph E. Elmquist^{⊗,1} David B. Newell,¹ David Goldhaber-Gordon,^{2,3,*} and Albert F. Rigosi^{⊗,1,†}

¹Physical Measurement Laboratory, National Institute of Standards and Technology (NIST), Gaithersburg, Maryland 20899, USA


²Department of Physics, Stanford University, Stanford, California 94305, USA

³Stanford Institute for Materials and Energy Sciences, SLAC National Accelerator Laboratory, Menlo Park, California 94025, USA

⁴Department of Applied Physics, Stanford University, Stanford, California 94305, USA

⁵Department of Materials Science and Engineering, Stanford University, Stanford, California 94305, USA

⁶Department of Electrical Engineering, University of California, Los Angeles, California 90095, USA

 (Received 19 March 2022; revised 20 July 2022; accepted 29 July 2022; published 2 September 2022)

Efforts to make the International System of Units (SI) more accessible have been growing since the global redefinition of the SI in 2019. Presently, the ohm is defined through the quantum Hall effect (QHE). However, quantum Hall devices require strong magnetic fields for a robust expression of the QHE. Magnetically doped topological insulators offer an opportunity to circumvent this limitation, as they require no magnetic field to provide a quantized resistance plateau via the quantum anomalous Hall effect (QAHE). Here, we detail experimental methodology and noise-analysis techniques for high-precision measurements of QAHE devices.

DOI: [10.1103/PhysRevApplied.18.034008](https://doi.org/10.1103/PhysRevApplied.18.034008)

I. INTRODUCTION

Since the redefinition of the International System of Units (SI) took place in 2019, many efforts have focused on the simplification of measurements so that the new SI, based on quantum phenomena, is accessible to sectors beyond government and metrology institutes [1–7]. For resistance metrology, this handoff manifests as the development of graphene-based quantum Hall effect (QHE) standards, with devices capable of accessing a quantized Hall resistance at higher temperatures and lower magnetic fields than the GaAs-based devices used previously. As a result, measurement techniques have become more user friendly due to simplified equipment infrastructure and longer device shelf life [6,8–10]. Despite the success of graphene-based QHE devices, operation constraints remain. Principally, the requirement for a strong magnetic field, at least 3.5 T [1], necessitates expensive equipment

to make metrology measurements. Materials like magnetically doped topological insulators (MTIs) offer access to the quantum anomalous Hall effect (QAHE) without a high-magnetic-field requirement [11–13]. In transport, the QAHE is observed as quantized transverse resistivity, $\rho_{xy} = h/e^2$, and zero longitudinal resistivity, $\rho_{xx} = 0$, even at zero applied magnetic field (although a small training field is generally required to initialize a magnetized state).

In three-dimensional topological insulators, strong spin-orbit coupling gives rise to an insulating bulk and topologically protected Dirac-like surface states. When doped with certain magnetic transition elements and ferromagnetically magnetized out of plane, these surface states feature a topologically nontrivial magnetic exchange gap. This energy gap closes where the component of magnetization normal to the surface changes direction. For samples that approach the two-dimensional limit and have uniform out-of-plane magnetization, such a transition occurs at the edge of the sample, since the surface-normal component of magnetization reverses sign between the top and bottom surfaces. A single one-dimensional chiral mode is localized along this edge, which is connected to the Hall conductivity, $\sigma_{xy} = 1/\rho_{xy} = e^2/h$.

Presently, the QAH state in MTI thin films is limited by the stringent operating temperatures required to minimize

*goldhaber-gordon@stanford.edu

†albert.rigosi@nist.gov

Published by the American Physical Society under the terms of the [Creative Commons Attribution 4.0 International](https://creativecommons.org/licenses/by/4.0/) license. Further distribution of this work must maintain attribution to the author(s) and the published article's title, journal citation, and DOI.

longitudinal conduction and achieve quantization of ρ_{xy} , with the best results being achieved for temperatures below 50 mK [14–17]. The development of modulation doping in TI thin films, where magnetic-dopant-rich layers sandwich minimally (or completely) undoped TI layers greatly improves the quality of MTI films, with one film showing quantization of ρ_{xy} to within 3% of h/e^2 at 2 K [18]. As advancements in growth techniques enable operation at more easily reachable temperatures, the QAHE could become the basis for a future resistance standard because, whereas operation of QHE standards requires superconducting electromagnets, QAHE devices need only a small permanent magnet to activate quantized resistances [17].

This work presents precision measurement techniques, results, and noise analyses of the h/e^2 -quantized Hall resistance in a modulation-doped sample of the MTI Cr-doped $(\text{BiSb})_2\text{Te}_3$ and gives them context by comparing them to other recent results [14–17]. Additionally, threshold currents for the breakdown of the QAH state and longitudinal resistivity behaviors are analyzed to better understand how one should expect MTI-based devices to perform. Accompanying uncertainty budgets are described and show that MTIs can be applied as standards in the near future, despite stringent temperature requirements. Taken together, this work serves to explore the possibility of using MTIs for resistance metrology [16]. Ultimately, MTI-based devices can be combined in a single system with Josephson voltage standards to obtain an alternative quantum current standard [19–21].

II. EXPERIMENTAL AND NUMERICAL METHODS

A. Sample preparation

The MTI film used in this work is grown in an ultrahigh-vacuum Perkin-Elmer molecular-beam-epitaxy system [22,23]. The growth of the six-quintuple-layer (QL) high-quality thin film takes place on a semi-insulating GaAs (111) B substrate, which is loaded into the chamber and preannealed to 630 °C in a Te-rich environment to remove any native oxides. During the growth process, the GaAs substrate temperature is maintained at 200 °C with the Bi, Sb, Te, and Cr sources all simultaneously evaporating. The top and bottom layers of the modulation-doped structure [18] are Cr-rich $(\text{Cr}_{0.24}\text{Bi}_{0.22}\text{Sb}_{0.54})_2\text{Te}_3$. These two single QLs surround four QLs of $(\text{Cr}_{0.12}\text{Bi}_{0.26}\text{Sb}_{0.62})_2\text{Te}_3$. The growth is monitored by reflection high-energy electron diffraction. After growth is complete and the sample is taken out of the chamber, a layer of poly(methyl methacrylate) is spin-coated to protect its surface.

MTI-based devices are patterned using direct-write optical photolithography. Every patterning step involves the coating of a hexamethyldisilazane adhesion layer and

a Megaposit SPR 3612 photoresist layer, with a pre-exposure bake at 80 °C for 120 s. The photoresist layer is subsequently exposed under a 385-nm light-emitting diode ultraviolet-light source with a dose of approximately 100 mJ/cm² and then developed in Microposit CD-30 for 35 s.

After the device mesa is defined with photolithography, Ar-ion milling is used to etch the Hall bar device. A micrograph of the 100- μm -wide Hall bar is provided in Fig. 1(a); the device features two pairs of voltage probes separated by 200 μm from center to center. The electrical contact pads consist of a 5-nm Ti adhesion layer and 100-nm Au deposited sequentially via electron-beam evaporation after 10-s *in situ* Ar pre-etching to remove surface impurities. To implement a top gate, a seed layer of 1 nm of Al is first uniformly deposited. This thin layer is oxidized in air before depositing approximately 40 nm of alumina through low-temperature (60 °C) atomic layer deposition using trimethylaluminum and water precursors. Finally, the top gate is deposited by evaporating 5-nm Ti and 85-nm Au after 10-s *in situ* Ar pre-etching. Excess alumina is removed using CD-26.

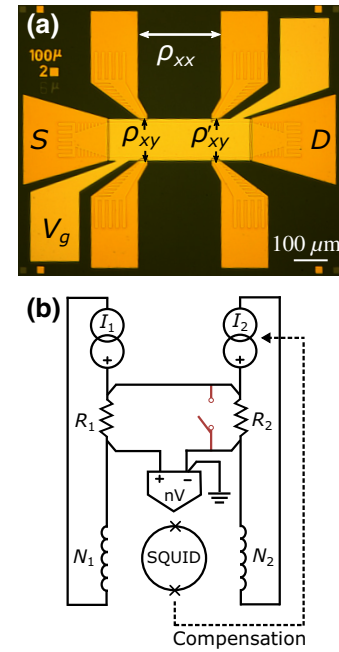


FIG. 1. (a) Micrograph of the QAHE device is shown. Current is sourced from the left contact (S) and drained on the right (D). Voltage terminals used to measure longitudinal and Hall resistivities are indicated. Gate voltage, V_g , is used to tune the Fermi level. (b) Simplified schematic of the CCC is provided. For longitudinal measurements, R_2 is shorted (red switch), so the CCC’s nanovoltmeter can be used independently. For measurements of ρ_{xy} and ρ'_{xy} , $N_1 = 2065$, $N_2 = 8$, R_2 is a 100- Ω standard, and R_1 is the QAHE device.

B. Transport and quantization measurements

The device is measured in a Bluefors dilution refrigerator with a base temperature of 10 mK. The sample is initially magnetized using a 1-T out-of-plane field (corresponding to $M = +1$ magnetization), but all measurements presented here are performed at zero field.

For precision measurements of the MTI Hall device, a 12-bit binary cryogenic current comparator (CCC) is used [24,25]. A CCC realizes an unknown resistance ratio, R_1/R_2 , from the inverse ratio of the currents I_1 and I_2 . It consists of a superconducting toroidal screen, which houses the superconducting windings N_1 and N_2 . When a current is passed through these windings, a net current, $|N_1 I_1 - N_2 I_2|$, exists on the surface of the superconducting screen due to the Meissner effect. The magnetic flux due to this net current imbalance is detected using a superconducting quantum interference device (SQUID). To eliminate thermoelectric offsets caused by linear thermal drifts, the currents, I_1 and I_2 , are reversed every half-cycle. Excluding weighted averages, all data points in this work reflect averages of 20–100 full cycles, where each full cycle lasts 60 s. Half-cycles consist of 30 samples, the first 14 of which are ignored to allow for stabilization after current reversal.

Orthogonal Hall measurements are conducted by comparing the MTI-based Hall device against a calibrated 100- Ω standard resistor, which is kept in a $25.000 \text{ }^\circ\text{C} \pm 0.003 \text{ }^\circ\text{C}$ temperature-controlled oil bath. For these measurements, $N_1 = 2065$, $N_2 = 8$, $R_2 = 100 \text{ } \Omega$, and R_1 is the QAH device with a nominal resistance of h/e^2 . The 100- Ω standard resistor is calibrated against NIST's quantum Hall resistance standard using a CCC. For the duration of this work, the drift of the 100- Ω standard resistor is $32.7 \text{ (n}\Omega/\Omega\text{)}/\text{yr}$. Longitudinal measurements are performed using the CCC's nanovoltmeter by shorting R_2 .

III. LONGITUDINAL AND HALL BEHAVIORS

The longitudinal resistivity is defined as $\rho_{xx} = (w/l) |R_{xx}|$, where w and l are the width of the device and center-to-center length between voltage terminals, respectively, and R_{xx} is the longitudinal resistance of the device, calculated by dividing the output of the CCC's nanovoltmeter by the applied current. Figure 2(a) shows ρ_{xx} as a function of gate voltage, V_g , for currents between 25 and 300 nA, with error bars representing 1σ type-A uncertainty. Adjusting the gate voltage tunes the Fermi level through the magnetic exchange gap. At the lowest currents, for gate voltages between $V_g = [-0.3 \text{ V}, 0.5 \text{ V}]$, ρ_{xx} is minimized to within the uncertainty of the measurement. The gate voltages that minimize ρ_{xx} correspond to the Fermi level being near the center of the magnetic exchange gap. As the gate voltage is tuned outside the optimal range, ρ_{xx} increases for all values of applied current, presumably due to charge carriers populating the dissipative surface states.

Figure 2(b), which replots a subset of data from Fig. 2(a) as a function of current bias [26,27], shows that ρ_{xx} varies nonlinearly with applied current. Although ρ_{xx} is minimized by reducing current bias, the associated uncertainty increases at low currents due to the reduction in overall signal magnitude. Within measurement uncertainty, the

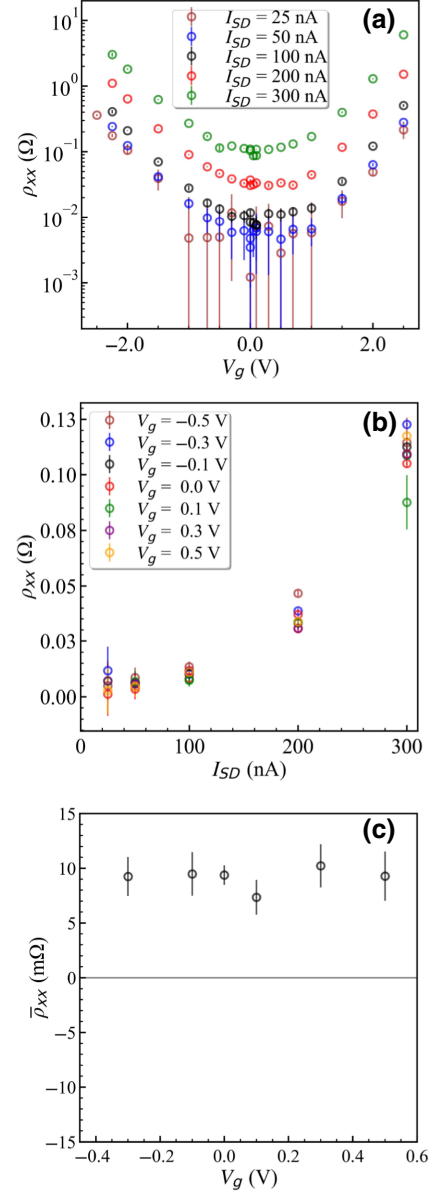


FIG. 2. (a) Longitudinal resistivity, ρ_{xx} , is examined as a function of gate voltage, V_g , for different values of bias current. All error bars represent 1σ uncertainty and are omitted when smaller than the data points. (b) ρ_{xx} plotted as a function of bias current, I_{SD} , for gate voltages between $V_g = -0.5 \text{ V}$ and $V_g = 0.5 \text{ V}$. Above 100 nA, breakdown of the QAH state is observed as a rapid increase in ρ_{xx} . (c) Weighted-average longitudinal resistivity, $\bar{\rho}_{xx}$, plotted as a function of gate voltage. Between $V_g = -0.3 \text{ V}$ and $V_g = 0.5 \text{ V}$, $\bar{\rho}_{xx}$ is minimized to within the uncertainty of the measurement.

minima of ρ_{xx} are equal for currents less than 100 nA when the gate voltage is within the range $V_g = [-0.3 \text{ V}, 0.5 \text{ V}]$. For currents above 100 nA, an offset in the minimum value of ρ_{xx} can be seen in Fig. 2(a). This offset indicates that current-induced breakdown of the device has begun [14,15,26]. The effect of breakdown can be seen more clearly in Fig. 2(b), as a nonlinear increase in ρ_{xx} is observed with increasing current. Similar to other works documenting the breakdown of the QAH state [14,15,28], breakdown occurs rapidly but is distinct from the step-like behavior often reported in QH devices [26]. The more gradual nature of breakdown is likely due to the large number of localized in-gap states present in QAH materials [15,28].

To fully characterize the longitudinal resistivity and optimize the gate voltage, weighted averages of data shown in Fig. 2(b) are taken. The weighted average at each value of gate voltage, $\bar{\rho}_{xx}$, is given by

$$\bar{\rho}_{xx} = \frac{\sum_{i=1}^n \rho_{xx}(I_i) / \sigma_i^2}{\sum_{i=1}^n 1 / \sigma_i^2} \quad (1)$$

where $\rho_{xx}(I_i)$ is the longitudinal resistivity measured at I_i and σ_i is the standard uncertainty of $\rho_{xx}(I_i)$. These weighted averages are plotted as a function of gate voltage in Fig. 2(c). Over the limited gate voltage range

$[-0.3 \text{ V}, 0.5 \text{ V}]$, the measured values are consistent to within 1σ type-A uncertainty, so the gate voltage cannot be further optimized. All subsequent measurements are taken with $V_g = 0.1 \text{ V}$, which is the midpoint of this interval.

Hall resistivities are measured to quantify $\delta\rho_{xy} = (R_{xy} - (h/e^2))/h/e^2$, the deviation of the measured Hall resistivities from the nominal value of the von Klitzing constant, $R_K = h/e^2$ (note that in two dimensions $R_{xy} = \rho_{xy}$). Figure 3(a) shows $\delta\rho_{xy}$ of the left pair of orthogonal contact pads measured for applied currents ranging from 50 to 500 nA. The measured Hall deviations of the right pair of orthogonal contacts, $\delta\rho'_{xy}$, are shown in Fig. 3(b) for applied currents of 50 and 100 nA. The difference between the two sets of Hall pairs can be seen in Fig. 3(c), which shows $\delta\rho_{xy}$ and $\delta\rho'_{xy}$ over the optimal gate-voltage range. For all currents, $|\delta\rho_{xy}| < |\delta\rho'_{xy}|$, suggesting that material or contact inhomogeneities are present. Over the gate-voltage range that optimizes ρ_{xx} [that in Fig. 2(c)], $\delta\rho_{xy}$ is consistently less than one part in 10^6 .

Figure 3(d) shows a subset of data from Fig. 3(a) plotted as a function of bias current. Interestingly, deviations of the Hall resistivity are less than two parts in 10^6 for currents up to 700 nA, despite the device having surpassed the onset of breakdown. The slow deviation of the Hall resistivity as a function of bias current is observed in previous studies of uniformly doped samples [15].

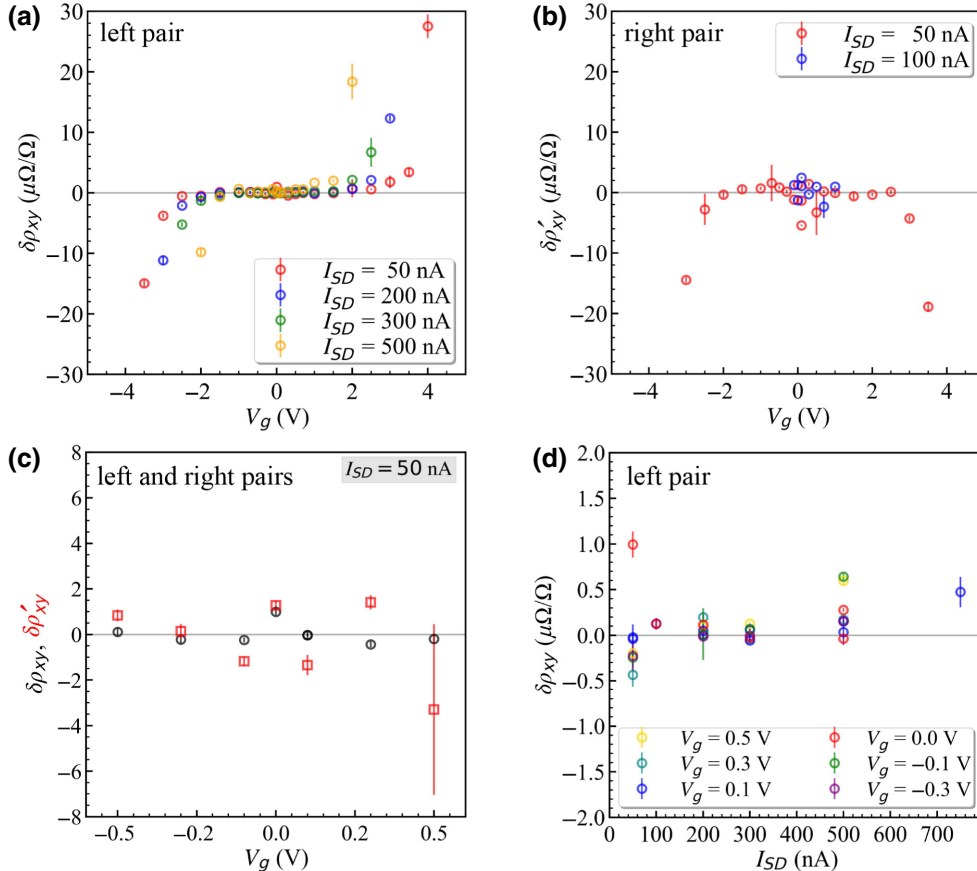


FIG. 3. (a) Deviations of the Hall resistivity from quantization, $\delta\rho_{xy}$ (measured using the left pair of orthogonal contacts), are shown as a function of gate voltage and for multiple values of bias current. (b) Deviations of the right pair of orthogonal contacts, $\delta\rho'_{xy}$, as a function of gate voltage for two values of applied current. (c) Magnified plot of 50-nA data shown in (a),(b) is shown for better comparison of $\delta\rho_{xy}$ (black circles) and $\delta\rho'_{xy}$ (red squares) over the optimal range of V_g . (d) $\delta\rho_{xy}$ is shown as a function of bias current, I_{SD} , for various gate voltages. Notably, $|\delta\rho_{xy}| < 2 \times 10^{-6}$ is observed, even after the onset of breakdown (i.e., for $I_{SD} > 100$ nA). All error bars indicate 1σ type-A uncertainty and may be smaller than some of the data points.

IV. RESULTS FROM NOISE ANALYSES

A. Noise measurements for the QAHE and standard resistor

A number of studies demonstrate impressive precision measurements of the quantization of the Hall voltage in MTI-based devices [14–17], with results improving rapidly over the past five years largely due to improved material quality [17,18]. As improved materials are measured with increasing precision, we must adopt improved error analysis techniques to allow the accurate determination and comparison of limiting experimental factors.

In cases where the dominant form of noise is white (random and uncorrelated) noise, the standard deviation of the mean takes the usual form

$$\bar{\sigma} = \frac{\sigma}{\sqrt{n}}, \quad (2)$$

where σ is the standard deviation of the measured value, and n is the number of samples. If the noise is correlated, then the uncertainty in the experiment must be assessed using alternative methods [29].

To determine whether Eq. (2) is applicable for a given measurement, a complete evaluation of the noise processes involved in the said measurement must be performed. A common method used in metrology is calculation of the Allan variance, σ_y^2 , which provides a measure of how the stability of a signal evolves over time [29,30]. For instantaneous samplings of a quantity, $x(t)$, at time t , the Allan variance is based on second differences: $x_{i+2} - 2x_{i+1} + x_i$. For M finite measurements of $x(t) = x_k$ for $k = 1, 2, \dots, M$ sampled at a measurement frequency τ_0 , the Allan variance $\sigma_y^2(\tau_0)$ is given by

$$\sigma_y^2(\tau_0) = \frac{1}{2\tau_0^2(M-2)} \sum_{k=1}^{M-2} (x_{k+2} - 2x_{k+1} + x_k)^2. \quad (3)$$

As it is the dependence on τ , the time between samples, which gives insight into noise processes, one can generalize Eq. (3) by letting $\tau = n\tau_0$ and averaging the second differences corresponding to this larger interval [29]:

$$\sigma_y^2(\tau) = \frac{1}{2\tau^2(M-2n)} \sum_{k=1}^{k=M-2n} (x_{k+2n} - 2x_{k+n} + x_k)^2. \quad (4)$$

As the standard deviation is the square root of the variance, the Allan deviation, σ_y , is equal to the square root of the Allan variance. The magnitude of the Allan deviation not only provides information on measurement stability, with low σ_y indicating strong stability, but the variation of σ_y with τ can help differentiate between different noise processes. For instance, the Allan deviation of a white-noise-limited process will scale as $\tau^{-1/2}$, while $1/f$ noise

is associated with constant Allan deviation. Furthermore, it is crucial that one understands the long-term stability and correlation of measurements to ensure that the type-A uncertainty can be reduced by averaging a larger number of measurements over a longer period of time.

The Allan deviation, σ_y , for the left pair of orthogonal contact pads is determined at two applied currents, 50 nA (red) and 300 nA (green), as shown in Fig. 4(a). While part-per-million quantization of the Hall resistivity is accessible at both 50 and 300 nA [see Fig. 3(d)], we find a substantial difference in the noise correlations of the measurements at these two currents. The 50-nA signal is white-noise limited up to $\tau \sim 2 \times 10^3$ s, while the 300-nA signal deviates

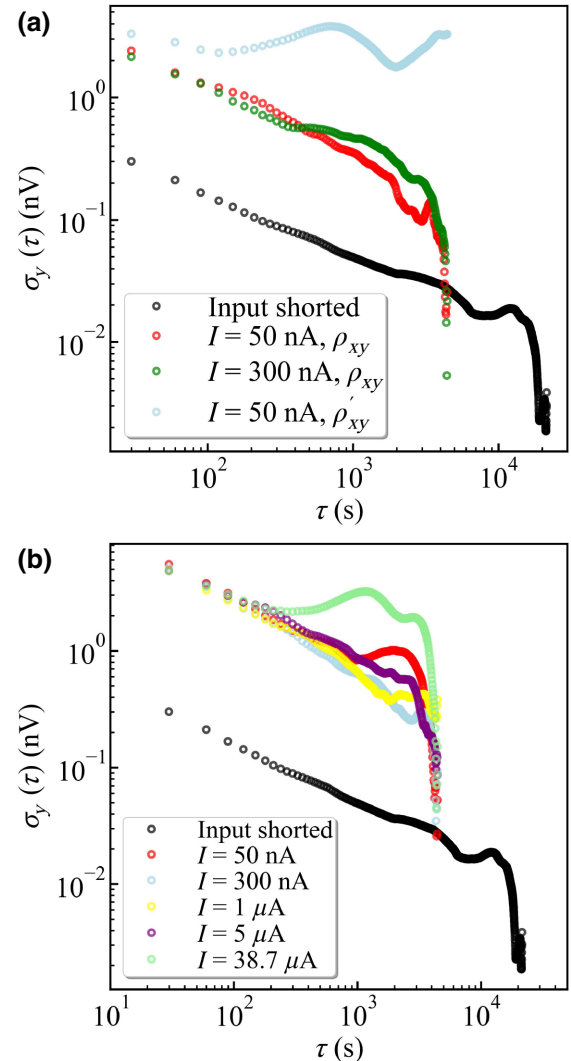


FIG. 4. (a) Allan deviation, σ_y , calculated for 50- and 300-nA measurements of $\delta\rho_{xy}$ and for the 50-nA measurement of $\delta\rho'_{xy}$, as a function of the averaging time, τ . (b) Allan deviation for the 25.8-k Ω standard resistor measured at 50 nA (red), 300 nA (cyan), 1 μ A (yellow), 5 μ A (purple), and 38.74 μ A (green) as a function of the averaging time, τ . Black circles, shown in both (a),(b), give the baseline noise associated with CCC's nanovoltmeter.

from white-noise behavior, $\sigma_y \sim \tau^{-1/2}$, at $\tau \sim 3 \times 10^2$ s. From this difference, we can learn to what extent noise limits the accuracy of our measurements. This noise analysis indicates that, despite raw transport evaluations of $\delta\rho_{xy}$ appearing to be similar at 300 and 50 nA ($\delta\rho_{xy} < 1 \times 10^{-6}$ for both), the type-A uncertainty of the measurements made at 300 nA cannot be reduced by averaging for an arbitrarily long amount of time or even by averaging for times that are reasonable at 50 nA. A clue to the origin of the lower stability at 300 nA can be found in our evaluation of ρ_{xx} as a function of current bias. We know that by 300 nA the system surpasses the onset of breakdown [Fig. 2(b)] and dissipative processes are occurring in the bulk of the device [28]. These processes, which are not present at 50 nA, may be contributing to the observed long-term correlations.

A similar analysis is performed on the second orthogonal pair [used to measure $\delta\rho'_{xy}$ of Fig. 3(b)], and the corresponding Allan deviation for 50-nA data may be seen in blue in Fig. 4(a). Not only is the magnitude of σ_y greater for the second orthogonal pair than the first, but the signal is white-noise limited only for $\tau < 1 \times 10^2$. The noise analysis therefore supports what is observed in transport [Fig. 3(c)]—the first pair of orthogonal contacts provides higher-quality measurements than the second, regardless of bias current, likely due to device or material inhomogeneities.

To further understand the limitations of the measurements presented in this study, a baseline assessment of the stability of the nanovoltmeter is performed and is shown in both plots of Fig. 4. For this measurement, both input terminals of the CCC’s nanovoltmeter are shorted, bypassing the QAH sample. Interestingly, the Allan deviation of the baseline signal is nearly an order of magnitude lower than any measurement of the QAH device, as seen in Fig. 4(a).

To determine whether the increased type-A noise observed during the Hall measurements is associated specifically with the QAH device or is a generic feature of the measurement setup as a whole, an independent analysis of the noise for a room-temperature 25.8-k Ω standard resistor is conducted. Because the 25.8-k Ω standard resistor is at room temperature, the analysis below does not include the QAH device or tertiary noise sources, such as triboelectric noise from measurement lines inside the cryostat. Five currents are used, 50 nA (red), 300 nA (blue), 1 μ A (yellow), 5 μ A (purple), and 38.74 μ A (green), and the associated Allan deviations are shown in Fig. 4(b). Here, we note that the difference in the qualitative behavior for the largest value of bias current could be a result of drift or a byproduct of self-heating of the resistor due to the large bias current. Regardless, a similar magnitude of σ_y is found for all measurements of the 25.8-k Ω standard resistor as compared to the QAH device. This indicates that the large type-A uncertainty is a feature of the measurement setup, not a limitation of the QAH device

itself. The source of this offset in the measurement setup is still under investigation, but possible contributing factors are the signal-to-noise ratio [17] and stability of the current source.

B. Uncertainty budget

A summary of the precision measurements of $\delta\rho_{xy}$ and ρ_{xx} is shown in Figs. 5(a) and 5(b), respectively, with

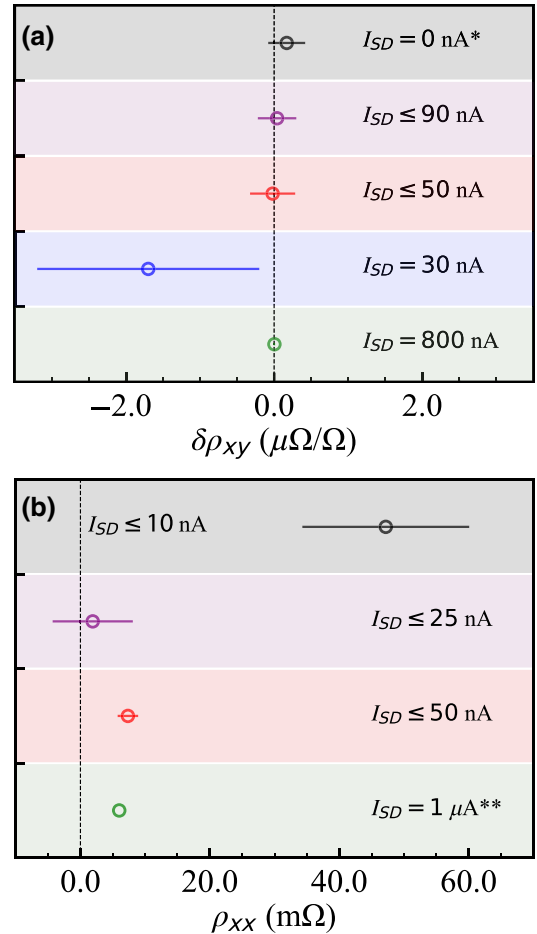


FIG. 5. Summary of the precision measurements made on MTI devices in the QAH state since 2018. (a) $\delta\rho_{xy}$ is the deviation of the Hall resistivity from quantization. (b) ρ_{xx} is the lowest reported longitudinal resistivity. Applied currents vary and the following measurements are represented: 2018 NIST-Stanford (purple, $\delta\rho_{xy} = 0.04 \mu\Omega/\Omega \pm 0.26 \mu\Omega/\Omega$ and $\rho_{xx} = 1.9 \text{ m}\Omega \pm 6.2 \text{ m}\Omega$) [15], 2018 PTB-UW (black, $\delta\rho_{xy} = 0.17 \mu\Omega/\Omega \pm 0.25 \mu\Omega/\Omega$ and $\rho_{xx} = 47.2 \text{ m}\Omega \pm 12.9 \text{ m}\Omega$) [14], the results of the present study (red, $\delta\rho_{xy} = -0.02 \mu\Omega/\Omega \pm 0.31 \mu\Omega/\Omega$ and $\rho_{xx} = 7.34 \text{ m}\Omega \pm 1.60 \text{ m}\Omega$), 2020 NMIJ and partners [blue, $\delta\rho_{xy} = -1.7 \mu\Omega/\Omega \pm 1.5 \mu\Omega/\Omega$ and $\rho_{xx} = 3.5 \Omega \pm 1 \Omega$; note that this value of ρ_{xx} is not shown in (b) because it is off scale] [16], and 2022 NMIJ and partners (green, $\delta\rho_{xy} = 0.004 \mu\Omega/\Omega \pm 0.01 \mu\Omega/\Omega$ and $\rho_{xx} \sim 6 \text{ m}\Omega$) [17]. * Value extrapolated to $I_{SD} = 0$ nA using power-law fit to data obtained for currents ranging from 5 to 50 nA. ** Precise error bars are not given in the text for these data, and therefore, are not represented.

TABLE I. The total uncertainty budget is shown. The factors influencing type-B uncertainties include finite dissipation from the MTI-based device, the CCC, and finite leakage resistances of the cables and connectors. Other type-B uncertainties include ratio errors, quantization errors, and calibration errors from the standard resistor.

Parameter	Type	$u_i (k=1) (\mu\Omega/\Omega)$
Statistics	A	0.064
Leakage	B	0.298
Ratio of the CCC winding	B	0.0002
Quantization errors in analog-to-digital conversion	B	0.001
Resistance standard	B	0.003
Combined	RSS	0.305

data also including summarizing points from other metrological measurements of QAH devices. Applied currents vary and the following MTI measurements are represented: 2018 National Institute of Standards and Technology (NIST) and Stanford University (purple) [15], Physikalisch-Technische Bundesanstalt (PTB) and University of Würzburg (black) [14], this work's device (red), 2020 National Metrology Institute of Japan (NMIJ) and partners (blue) [16], and 2022 NMIJ and partners (green) [17]. Error bars for data representing our present study represent $k=1$ type-A and -B combined uncertainties. Some measurements feature elevated ρ_{xx} values without obvious correlations to ρ_{xy} . This behavior echoes what is observed at the onset of breakdown where $\delta\rho_{xy}$ remains small, despite a rapid increase in ρ_{xx} . Given that ρ_{xx} appears to be a more sensitive probe than $\delta\rho_{xy}$, the higher longitudinal resistivity could stem from measurement conditions (for example, higher electron temperatures in one cryostat compared to another) or could be an indication of overall sample quality.

Table I provides a summary of the full uncertainty budget for this experimental work with the combined type-A uncertainty listed in row one (see the Supplemental Material [31]). The factors influencing the type-B uncertainties are listed in the remaining rows of Table I and include contributions due to finite leakage resistances of the cables and connectors, ratio errors, quantization errors, and calibration errors from the standard resistor. The total combined uncertainty is found by calculating a residual sum of squares (RSS). To calculate the type-A statistics for these uncertainty budgets, a total of 330 and 130 measurements are performed for the Hall and longitudinal resistances, respectively.

V. CONCLUSIONS

This work presents results on precision measurements and noise-analysis techniques for analyzing the h/e^2 -quantized plateau of the quantum anomalous Hall effect.

The modulation-doped structure of the MTI film helps to improve this measurement from our previous work [15]. Modulation doping is shown to improve the spatial uniformity of the magnetic exchange gap in Cr bismuth antimony telluride samples, leading to a larger exchange gap on average (see the Supplemental Material [31]). Improvements for future devices could include the implementation of superconducting contacts to reduce potential excess resistance from quantum Hall hotspots, as has been done with graphene-based resistance standards [32]. Additionally, standards of various resistance values, including $h/2e^2$, could be realized through the creation of magnetic domains within a single QAHE device, although highly quantized resistances have yet to be demonstrated in such a scheme [33,34]. The analysis techniques and measurements discussed here will help to establish experimental protocols that optimize precision and elucidate future limitations to measurement capabilities of MTI-based devices as the metrology community begins to increase its attention and efforts towards topological materials.

ACKNOWLEDGMENTS

The authors would like to thank S. Mhatre, A. Levy, G. Fitzpatrick, and E. C. Benck for their assistance in the NIST internal review process. L.K.R., I.T.R., M.P.A., and D.G.-G. acknowledge support by the Department of Energy, Office of Science, Basic Energy Sciences, Materials Sciences and Engineering Division, under Contract No. DE-AC02-76SF00515 for device fabrication, characterization, and measurement. Part of this work is performed at the Stanford Nano Shared Facilities (SNSF) and the Stanford Nanofabrication Facility (SNF), supported by the National Science Foundation under Grant No. ECCS-2026822. L.T. and K.L.W. acknowledge support from the National Science Foundation (NSF) (Grants No. DMR-1411085 and No. DMR-1810163) and the Army Research Office Multidisciplinary University Research Initiative (MURI) under Grants No. W911NF16-1-0472 and No. W911NF-19-S-0008 for materials synthesis. Work presented herein is performed, for a subset of the authors, as part of their official duties for the United States Government. Funding is hence appropriated by the United States Congress directly.

The authors declare no competing interest. Commercial equipment, instruments, and materials are identified in this paper in order to specify the experimental procedure adequately. Such identification is not intended to imply recommendation or endorsement by the National Institute of Standards and Technology or the United States Government, nor is it intended to imply that the materials or equipment identified are necessarily the best available for the purpose.

- [1] R. Ribeiro-Palau, F. Lafont, J. Brun-Picard, D. Kazazis, A. Michon, F. Cheynis, O. Couturaud, C. Consejo, B. Jouault, W. Poirier, and F. Schopfer, Quantum Hall resistance standard in graphene devices under relaxed experimental conditions, *Nat. Nanotechnol.* **10**, 965 (2015).
- [2] A. Tzalenchuk, S. Lara-Avila, A. Kalaboukhov, S. Paolillo, M. Syväjärvi, R. Yakimova, O. Kazakova, T. J. Janssen, V. Fal'Ko, and S. Kubatkin, Towards a quantum resistance standard based on epitaxial graphene, *Nat. Nanotechnol.* **5**, 186 (2010).
- [3] M. Woszczyzna, M. Friedemann, M. Götz, E. Pesel, K. Pierz, T. Weimann, and F. J. Ahlers, Precision quantization of Hall resistance in transferred graphene, *Appl. Phys. Lett.* **100**, 164106 (2012).
- [4] J. Kučera, P. Svoboda, and K. Pierz, Precision quantization of Hall resistance in transferred graphene, *IEEE Trans. Instrum. Meas.* **68**, 2106 (2018).
- [5] T. Oe, A. F. Rigosi, M. Kruskopf, B.-Y. Wu, H.-Y. Lee, Y. Yang, R. E. Elmquist, N.-H. Kaneko, and D. G. Jarrett, Comparison between NIST graphene and AIST GaAs quantized Hall devices, *IEEE Trans. Instrum. Meas.* **69**, 3103 (2019).
- [6] T. J. B. M. Janssen, S. Rozhko, I. Antonov, A. Tzalenchuk, J. M. Williams, Z. Melhem, H. He, S. Lara-Avila, S. Kubatkin, and R. Yakimova, Operation of graphene quantum Hall resistance standard in a cryogen-free table-top system, *2D Mater.* **2**, 035015-1-9 (2015).
- [7] A. F. Rigosi and R. E. Elmquist, The quantum Hall effect in the era of the new SI, *Semicond. Sci. Technol.* **34**, 093004 (2019).
- [8] H. He, K. H. Kim, A. Danilov, D. Montemurro, L. Yu, Y. W. Park, F. Lombardi, T. Bauch, K. Moth-Poulsen, T. Iakimov, and R. Yakimova, Uniform doping of graphene close to the Dirac point by polymer-assisted assembly of molecular dopants, *Nat. Commun.* **9**, 3956 (2018).
- [9] A. F. Rigosi, M. Kruskopf, H. M. Hill, H. Jin, B.-Y. Wu, P. E. Johnson, S. Zhang, M. Berilla, A. R. Hight Walker, C. A. Hacker, *et al.*, Gateless and reversible carrier density tunability in epitaxial graphene devices functionalized with chromium tricarbonyl, *Carbon* **142**, 468 (2019).
- [10] M. Kruskopf, A. F. Rigosi, A. R. Panna, M. Marzano, D. Patel, H. Jin, D. B. Newell, and R. E. Elmquist, Next-generation crossover-free quantum Hall arrays with superconducting interconnections, *Metrologia* **56**, 065002 (2019).
- [11] R. Yu, W. Zhang, H.-J. Zhang, S.-C. Zhang, X. Dai, and Z. Fang, Quantized anomalous Hall effect in magnetic topological insulators, *Science* **329**, 61 (2010).
- [12] Y. L. Chen, J.-H. Chu, J. G. Analytis, Z. K. Liu, K. Igarashi, H.-H. Kuo, X. L. Qi, S. K. Mo, R. G. Moore, D. H. Lu, *et al.*, Massive Dirac fermion on the surface of a magnetically doped topological insulator, *Science* **329**, 659 (2010).
- [13] J. G. Checkelsky, J. Ye, Y. Onose, Y. Iwasa, and Y. Tokura, Dirac-fermion-mediated ferromagnetism in a topological insulator, *Nat. Phys.* **8**, 729 (2012).
- [14] M. Götz, K. M. Fijalkowski, E. Pesel, M. Hartl, S. Schreyeck, M. Winnerlein, S. Grauer, H. Scherer, K. Brunner, C. Gould, and F. J. Ahlers, Precision measurement of the quantized anomalous Hall resistance at zero magnetic field, *Appl. Phys. Lett.* **112**, 072102 (2018).
- [15] E. J. Fox, I. T. Rosen, Y. Yang, G. R. Jones, R. E. Elmquist, X. Kou, L. Pan, K. L. Wang, and D. Goldhaber-Gordon, Part-per-million quantization and current-induced breakdown of the quantum anomalous Hall effect, *Phys. Rev. B* **98**, 075145 (2018).
- [16] Y. Okazaki, T. Oe, M. Kawamura, R. Yoshimi, S. Nakamura, S. Takada, M. Mogi, K. S. Takahashi, A. Tsukazaki, M. Kawasaki, and Y. Tokura, Precise resistance measurement of quantum anomalous Hall effect in magnetic heterostructure film of topological insulator, *Appl. Phys. Lett.* **116**, 143101 (2020).
- [17] Y. Okazaki, T. Oe, M. Kawamura, R. Yoshimi, S. Nakamura, S. Takada, M. Mogi, K. S. Takahashi, A. Tsukazaki, M. Kawasaki, and Y. Tokura, Quantum anomalous Hall effect with a permanent magnet defines a quantum resistance standard, *Nat. Phys.* **18**, 25 (2022).
- [18] M. Mogi, R. Yoshimi, A. Tsukazaki, K. Yasuda, Y. Kozuka, K. S. Takahashi, M. Kawasaki, and Y. Tokura, Magnetic modulation doping in topological insulators toward higher-temperature quantum anomalous Hall effect, *Appl. Phys. Lett.* **107**, 182401 (2015).
- [19] H. Scherer and B. Camarota, Quantum metrology triangle experiments: A status review, *Meas. Sci. Technol.* **23**, 124010 (2012).
- [20] M. W. Keller and J. Aumentado, A new era for the ampere, *Physics* **9**, 144 (2016).
- [21] Y. H. Tang, V. N. Ojha, S. Schlamminger, A. Rüfenacht, C. J. Burroughs, P. D. Dresselhaus, and S. P. Benz, A 10 V programmable Josephson voltage standard and its applications for voltage metrology, *Metrologia* **49**, 635 (2012).
- [22] X. Kou, S. T. Guo, Y. Fan, L. Pan, M. Lang, Y. Jiang, Q. Shao, T. Nie, K. Murata, J. Tang, *et al.*, Scale-Invariant Quantum Anomalous Hall Effect in Magnetic Topological Insulators beyond the Two-Dimensional Limit, *Phys. Rev. Lett.* **113**, 137201 (2014).
- [23] A. J. Bestwick, E. J. Fox, X. Kou, L. Pan, K. L. Wang, and D. Goldhaber-Gordon, Precise Quantization of the Anomalous Hall Effect Near Zero Magnetic Field, *Phys. Rev. Lett.* **114**, 187201 (2015).
- [24] D. Drung, M. Gotz, E. Pesel, H. J. Barthelmeß, and C. Hinrichs, Aspects of application and calibration of a binary compensation unit for cryogenic current comparator setups, *IEEE Trans. Instrum. Meas.* **62**, 2820 (2013).
- [25] M. Götz, D. Drung, E. Pesel, H. J. Barthelmeß, C. Hinrichs, C. Aßmann, M. Peters, H. Scherer, B. Schumacher, and T. Schurig, Improved cryogenic current comparator setup with digital current sources, *IEEE Trans. Instrum. Meas.* **58**, 1176 (2009).
- [26] B. Jeckelmann and B. Jeanneret, The quantum Hall effect as an electrical resistance standard, *Rep. Prog. Phys.* **64**, 1603 (2001).
- [27] F. Delahaye and B. Jeckelmann, Revised technical guidelines for reliable dc measurements of the quantized Hall resistance, *Metrologia* **40**, 217 (2003).
- [28] L. K. Rodenbach, I. T. Rosen, E. J. Fox, P. Zhang, L. Pan, K. L. Wang, M. A. Kastner, and D. Goldhaber-Gordon, Bulk dissipation in the quantum anomalous Hall effect, *APL Mater.* **9**, 081116 (2021).

- [29] D. W. Allan, Statistics of atomic frequency standards, *Proc. IEEE* **54**, 221 (1966).
- [30] T. J. Witt, Using the Allan variance and power spectral density to characterize dc nanovoltmeters, *IEEE Trans. Instrum. Meas.* **50**, 445 (2001).
- [31] See the Supplemental Material at <http://link.aps.org/supplemental/10.1103/PhysRevApplied.18.034008> for information on the magnetic gap and additional uncertainty budgets.
- [32] M. Kruskopf, A. F. Rigosi, A. R. Panna, M. Marzano, D. K. Patel, H. Jin, D. B. Newell, and R. E. Elmquist, Two-terminal and multi-terminal designs for next-generation quantized Hall resistance standards: Contact material and geometry, *IEEE Trans. Electron Dev.* **66**, 3973 (2019).
- [33] I. T. Rosen, E. J. Fox, X. Kou, L. Pan, K. L. Wang, and D. Goldhaber-Gordon, Chiral transport along magnetic domain walls in the quantum anomalous Hall effect, *npj Quantum Mater.* **2**, 1 (2017).
- [34] K. Yasuda, M. Mogi, R. Yoshimi, A. Tsukazaki, K. S. Takahashi, M. Kawasaki, F. Kagawa, and Y. Tokura, Quantized chiral edge conduction on domain walls of a magnetic topological insulator, *Science* **358**, 1311 (2017).